1   Seismic Analysis of the Gas Hydrate System at Pointer Ridge Offshore SW

2   Taiwan

3   Wei-Chung Han[1], Liwen Chen[2*], Char-Shine Liu[2], Christian Berndt[3], Wu-Cheng Chi[4]

4

5   *[1]Green Energy and Environment Research Laboratories, Industrial Technology Research*
6   *Institute, Taiwan*
7   *[2]Ocean Center, National Taiwan University, Taiwan*
8   *[3]Helmholtz Centre for Ocean Research Kiel, Germany*
9   *[4]Institute of Earth Sciences, Academia Sinica, Taiwan*
10
11   *Corresponding author
12   Email: mmammamma@gmail.com
13

14

15

16   Key words: gas hydrates, Taiwan, 3D seismic, seismic attributes, neural networks

17

18   **Abstract**

19   Pointer Ridge is a gas hydrate prospect on the South China Sea continental slope offshore SW

20   Taiwan. It is characterized by densely distributed bottom simulating reflections (BSRs), active gas

21   seepage, and potential sandy gas hydrate reservoirs. To understand how the fluids have migrated toward

22   the seafloor, and the role of geological processes in the gas hydrate system, we have collected and

23   analyzed high-quality 2D and 3D reflection seismic data. We first mapped the spatial distribution of the

24   BSRs, and interpreted a major normal fault, Pointer Ridge Fault (PR Fault). The NE-SW trending fault

25   dips to the east, and separates the erosional regime to the west from the depositional regime to the east.

26   One active vent site was identified directly above the PR Fault, while another is located on a topographic

27   high to the west of the fault. On the hanging block of the fault we found at least one major unconformity.

28   The seismic data indicate refilled channels with coarser-grained sediments in the hanging wall of the

29   normal fault. Seismic attribute analysis shows subsurface fluid conduits and potential gas hydrate

30   reservoirs. We propose two types of gas chimneys, which are separated by the fault. Gas plumes derived

31   from hydroacoustic data are mostly from the footwall block of the fault. We infer that fluid flow is more

32   active in the erosional environment compared to the depositional one, is the result of reduced

33   overburden. The methane-bearing fluids migrate upward along the PR Fault and chimneys and form

34   hydrates above the base of the gas hydrate stability zone. Based on seismic interpretation and seismic

35   attribute analysis, we postulate that the channel infill constitutes the most promising hydrate reservoirs

36   in this geological setting. In the surveyed area of Pointer Ridge these channels occur mainly below the

37   gas hydrate stability zone.

38

1. Introduction

Gas hydrates, a potentially vast energy resource, are ice-like solid materials composed of water and gas molecules, often formed in deep ocean sediments. Studying gas hydrate systems helps us to better understand marine resources, seafloor stability, and changes in the environment. Gas hydrates have been considered as a future energy resource in some countries, including the United States, Canada, Japan, India, Korea, China, and Taiwan. Dissociation of gas hydrates may contribute to submarine geohazards (Nixon & Grozic, 2007) and greenhouse gas release (Kvenvolden, 1998; Sloan, 1998; Ruppel, 2011; Berndt et al., 2014). The key issues that need to be considered while studying a gas hydrate system include: (1) the dynamics of the gas hydrate stability zone (GHSZ) where pressure and temperature conditions allow natural gas hydrate to form; (2) recent gas flux into the GHSZ along fluid conduits; and (3) the suitability of reservoirs, such as sediment type and fractures within the GHSZ (Collett, 2012; Max and Johnson, 2014).

In the region offshore SW Taiwan, gas hydrates have been extensively studied in recent years. Ubiquitous bottom simulating reflections (BSRs) that indicate the presence of gas hydrates have been observed in both the active and passive margins (Lundberg et al., 1992; Reed et al., 1992; Chi et al., 1998, 2006; Shyu et al., 1998; Schnurle et al., 1999; Chow et al., 2000; McDonnell et al., 2000; Liu et al., 2006; Lin et al., 2009; Chen et al., 2012; Lin et al., 2014). The gas hydrate investigation program, funded by the Central Geological Survey (CGS) of the Ministry of Economic Affairs, Taiwan, ROC identified several gas hydrate prospects, including Jiulong Ridge, Horseshoe Ridge, Pointer Ridge, Formosa Ridge and Palm Ridge, on the northern margin of the South China Sea (SCS) (Fig. 1). Gas hydrates were sampled at Jiulong Ridge and Horseshoe Ridge (Fig.1) by the Guangzhou Marine Geological Survey gas hydrate expeditions (GMGS2) (Zhang et al., 2014; 2015), while an active cold seep system was identified at Formosa Ridge (Chen et al., 2014; Feng and Chen, 2015; Hsu et al., 2017). Although densely distributed BSRs (Liu et al., 2006) and geochemical anomalies (Chuang et al., 2010) at Pointer Ridge suggest it is a good site for future gas hydrate exploitation, the geological controls on the gas hydrate system at Pointer Ridge are poorly understood.

65   This study elucidates how hydrocarbon-bearing fluids have migrated through conduits and

66   accumulated to form gas hydrate reservoirs at Pointer Ridge. As gas can only be produced commercially

67   from high-porosity and high-permeability sandy intervals (Johnson and Max, 2006), the identification

68   of sand-rich hydrate reservoirs is one of the most important issues for gas hydrate exploration.

69   Subsurface fluid conduits are major pathways that transport fluids into the GHSZ and then form gas

70   hydrates under favorable conditions. To understand the gas hydrate system in Pointer Ridge, we

71   analyzed 2D and 3D seismic data for structural and stratigraphic interpretations. Then detailed seismic

72   attribute analysis was applied to detect subtle features, such as paleo-channels and fluid conduits, from

73   the 3D seismic cube. Finally, the spatial distribution of fluid conduits and reservoirs was mapped and

74   used to construct a conceptual model of the Pointer Ridge gas hydrate system.

75

76   **2. Geologic background**

77   The area offshore SW Taiwan is situated in the incipient collision between the Eurasian continent

78   and the Luzon arc (Huang et al., 1997; Liu et al., 1997). The deformation front separates the active

79   Taiwan accretionary wedge to the east from the passive SCS continental slope to the west (Liu et al.,

80   1997; Yu, 2004; Han et al., 2017) (Fig. 1). Located west of the deformation front, the Tainan Basin has

81   experienced a rapid tectonic subsidence since the late Miocene (Ru and Pigott, 1986; Lin et al., 2003),

82   probably related to the tectonic evolution of the Dongsha and Taiwan blocks (Yu et al., 2012). A series

83   of ENE-trending normal faults (Yang et al., 1991; Liu et al., 1997) and graben/half-graben structures

84   (Yeh et al., 2012; Li et al., 2007; Lester et al., 2012; Liao et al., 2014; 2016) form the predominant

85   tectonic structures in this area. Growth strata related to a large normal fault strike along the northeastern

86   SCS shelf break and die out to the southwest near the Formosa Ridge (Fig. 1). This normal fault acts as

87   a major fluid conduit transporting thermogenic gas from deep-seated gas kitchens as suggested by Lin

88   et al. (1993) to the F-structure gas field in the north (Lin et al., 2009). In addition to faults, mud diapirs

89   transport gas from depth for the formation of gas hydrates in the Tainan Basin (Yan et al., 2006; Li et

90   al., 2013). Morphologically, the SCS slope is dissected by the Formosa Canyon, the Penghu Canyon,

91   the West Penghu Canyon, and several erosional gullies (Fig. 1) (Han, 2017). These submarine

4

92 canyons/channels are major conduits that transport significant amounts of sediment to the toe of the

93 SCS Slope where they are reworked by contourites and form sediment wave fields (Gong et al., 2012).

94 **3. Data and methodology**

95 The bathymetric map used in this study was derived from a 50 m resolution digital elevation model

96 offshore SW Taiwan following the procedures described in Liu et al. (1998). In this study, we use 2D

97 multi-channel seismic (MCS) reflection data to constrain the regional geologic framework and to image

98 deep structures. In addition, we analyzed a 3D seismic cube to constrain detailed spatial variations of

99 the geological features.

100 MCS data used in this study were collected from 2009 to 2015 by the R/V Ocean Researcher I (OR1)

101 and during the 2009 MGL0905 cruise of the R/V Marcus G. Langseth (MGL) (Fig. 2). Acquisition

102 parameters of the seismic survey systems used in this study are presented in Table 1. All the seismic

103 data were processed at the Institute of Oceanography, National Taiwan University, using ProMAX and

104 OpendTect. Typical seismic processing procedures followed the workflow proposed by Han et al.

105 (2017), including trace editing, geometry setup, band-pass filtering, amplitude correction, spike noise

106 removal, velocity analysis, normal moveout correction, water velocity F-K migration and water bottom

107 muting. Forty-eight closely spaced (100-m) 2D seismic lines were collected inside an area of

108 approximately 70.5 km^2 (4.7 km by 15 km) during a pseudo-3D seismic survey. The 2D seismic data

109 used to build the 3D seismic cube were collected by OR1 during the survey cruises OR1-1083 and OR1-

110 1089 (Table 1). By utilizing the streamer feathering, we filled in the large cross-line gaps following the

111 procedure proposed by Han (2017), and then processed the seismic data to obtain a 3D cube. The

112 processing flow included trace editing, band-pass filtering, amplitude correction, spike noise removal,

113 3D geometry setup, 3D velocity analysis, normal moveout correction, 3D stacking, and one pass water

114 velocity 2D F-K migration in inline direction. After that, a dip-steering medium filtering was applied

115 by using OpendTect remove high frequency noise (Brouwer and Huck, 2011; Qayyum & de Groot,

116 2012). The final 3D seismic cube (see Table 2 for geometry parameters) was then interpreted using

117 seismic attribute analysis.

118   We conducted a tectono-stratigraphic analysis of all available seismic data, particularly of seismic

119   features that may indicate hydrocarbon presence, such as fluid conduits and turbidite channel sands with

120   anomalous amplitudes. We applied multi-attribute analyses including co-blending of seismic attributes

121   and neural network technology to better detect critical geological features. Co-blending of seismic

122   attributes can visualize several seismic attributes at the same time and it has been introduced as a

123   powerful way to enhance the contrast between the geologic targets and the background (Taner, 2001;

124   Ferguson et al., 2010; Chopra and Marfurt, 2008; 2011; Barnes et al., 2011; Chinwuko et al., 2015).

125   The trained neural networks can generate probability cubes of interests such as "chimney cubes" or

126   "fault cubes" by building a neural network for seismic attributes at each position of the 3D seismic cube

127   (Meldahl et al., 2001; Ligtenberg, 2005; Tingdahl and De Rooij, 2005). "Chimney cube" shows the

128   probability of the vertical disturbance, while the "fault cube" indicates faults and fractures. The

129   attributes used for neural network training include energy, polar dip, polar dip variance, similarity,

130   reference time. These attributes are generally extracted from the traces surrounding the trace of

131   investigation. For details of the neural network processing procedure see Meldahl et al. (2001) and

132   Aminzadeh et al. (2002).

133

134   **4.   Results from seismic analysis**

135   Widely distributed BSRs (Fig. 3a), seafloor venting/seeps leakage (Fig. 4), and the presence of

136   subsurface fluid conduits (Fig. 4) suggest Pointer Ridge is a potential gas hydrate prospect. To better

137   understand the geologic features and the nature of the gas hydrate system, we used the IHS Kingdom

138   software of IHS and the OpendTect software dGB Earth Sciences for structural/stratigraphic

139   frameworks and seismic attribute analysis, respectively.

140

141   *4.1 Topographic and structural settings of the Pointer Ridge area*

142   The Pointer Ridge Fault (PR Fault) is a blind, NE-SW striking normal fault (Fig. 5) with a length

143   around 5.2 km (Fig. 2) based on available seismic data. Although there are growth strata and possibly

144   a maximum offset of 460 m across this fault (Fig. 5), there is no indication that it has deformed the

145   shallow sediments. Thus the PR Fault is not currently active. In addition to the PR Fault, minor normal

146   faults are also observed in the seismic data (Fig. 5).

147   The PR Fault separates the depositional and erosional settings at Pointer Ridge. Topographic (Figs.

148   2 and 3b) and seismic (Figs. 5 and 6) variations can be observed across the PR Fault. On the footwall,

149   irregular topography and chaotic seismic facies indicate erosion; whereas on the hanging wall, smooth

150   topography and stratified sediment reflections are linked to a relatively stable depositional regime. On

151   top of Pointer Ridge, several NE-SW trending gullies reveal that the paleo-activities of PR Fault may

152   lead to the present morphology in Pointer Ridge area.

153

154   *4.2 Seismic units and sedimentary features*

155   Three seismic units, including U_a, U_b and U_c, are identified in the study area. U_a is interpreted as the

156   oldest and U_c as the youngest unit that can be recognized from the seismic data. U_a is characterized by

157   weak, chaotic and discontinuous reflections with locally bright sections. U_b is characterized by

158   continuous, NW-dipping reflections with moderate to strong amplitudes that are truncated by the U_a to

159   the bottom and by the U_c to the top, respectively (Fig. 6). U_c consists of wavy, continuous reflections

160   with low to moderate amplitudes. Overall the seismic characteristics of U_b and U_c correlate with

161   stratified sediments, whereas the chaotic facies with poor seismic penetration of U_a may be caused by

162   more consolidated sediments. We interpret the unit with wavy reflections in U_c as contourite deposits.

163   The origin of the three seismic units is linked to the activity of the PR Fault. Growth strata observed in

164   U_b suggest that the sediments of U_b are syn-faulting deposits, while U_a and U_c are interpreted as pre-

165   faulting sediments and post-faulting sediments, respectively.

166   Since turbidite channel sands in the paleo-channel deposits have been suggested as the best

167   reservoirs for gas hydrate exploitation in deep sea environments (Johnson and Max, 2006; Bowswell et

168   al., 2016), it is crucial to map the location of paleo-channels using the 3D seismic cube in detail as these

169   promise the coarsest grain sizes. It has been suggested that using a seismic attribute alone is inefficient

170   to detect subsurface geologic features of a natural gas hydrate system (Ligtenberg, 2003). In addition,

171   Chinwuko et al. (2015) further suggests that co-blending of seismic attributes including the energy,

172 impedance, and the similarity can enhance, and thus allow more efficient interpretation of sandy channel

173 deposits. For example, the edge of the channels is often characterized by high energy, high impedance

174 contrast, and low similarity compared to the surrounding sediments. Therefore, besides conventional

175 seismic interpretation (Figs. 7a and 7b), co-blending of seismic attributes was applied to enhance the

176 edge of channel sand deposits (Figs. 7c and 7d.). The results show that paleo-channel cutting and filling

177 features exist both within and beneath the GHSZ (Figs. 7a and 7c). The paleo-channels in the GHSZ,

178 which could act as gas hydrate reservoirs, mostly occur in the footwall of the PR Fault, while in the

179 hanging wall of the PR Fault, paleo-channel deposits are generally below the BSR (Figs. 7b and 7d).

180 Figure 8 shows the distribution of paleo-channels that were identified in the GHSZ from the 3D seismic

181 cube.

182

183 *4.3 Seismic indicators of focused fluid flow*

184 Gas flares, carbonates (Figs. 5 and 6) and chimneys (Figs. 4; 6 and 9) indicate ongoing fluid flow

185 at Pointer Ridge (Fig. 4). Chimneys observed in seismic sections, which are widely accepted as

186 indications of active fluid conduits for focused flow, are characterized as low amplitude, chaotic vertical

187 disturbances (Berndt, 2005; Gay et al., 2006; 2012). Two types of chimneys are identified in the study

188 area (Fig. 10). Type I chimneys act as active fluid conduits for fluids migrating into the GHSZ and are

189 potentially linked to near-surface fluid migration structures, and even seepage at the surface, while type

190 II chimneys are buried by thick sediments and cannot lead to surface seepage (Fig. 9). The distribution

191 of chimneys shows that type I chimneys and gas flares mainly occur in the footwall of the PR Fault,

192 whereas type II chimneys occur mostly in the hanging wall (Fig. 2).

193 The distribution of gas flares implies that surface seepage may be linked to subsurface fluid

194 conduits (Fig. 4). To understand how gas-bearing fluids have migrated into the GHSZ and into the water

195 column, subsurface fluid conduits including chimneys and faults/fractures were detected by neural

196 networks based multi-attribute analysis. Fig. 11 illustrates how the neural network was trained to

197 generate the chimney cube. Firstly, chimneys were identified from conventional seismic profiles by the

198 interpreter (Fig. 11a). Then typical examples of "chimney" and "non-chimney" locations were picked

199 as the input for supervised neural network learning (Fig. 11b). Finally, the "chimney cube" was created

200 and compared to the conventional seismic cube (Figs. 11c; 11d and 11e). Subtle fluid conduits that are

201 difficult to identify from conventional seismic images are enhanced in the "chimney cube" (Figs. 11

202 and 12). The results reveal that fluid conduits in shallow sediments are more densely distributed in the

203 footwall than that in the hanging wall of the PR Fault (Fig. 12).

204

5. Discussion

5.1 Fluid flow behavior along faults

207 Extensional faults frequently act as conduits for focused fluid flow in passive margins worldwide.

208 For instance, focused fluid flow along polygonal fault systems are observed at the Norwegian margin

209 (Dalland et al., 1988; Berndt et al., 2003), Lower Congo Basin (Gay et al., 2004), South China Sea (Sun

210 et al., 2012) and North Sea (Lonerga et al., 1998). Li et al. (2013) suggest that basement-involved

211 normal faults transport mixed biogenic and thermogenic methane to the GHSZ, forming gas hydrates

212 in the Joulong Ridge area, South China Sea. In the Pointer Ridge area, the PR Fault also plays an

213 important role in transporting gas-bearing fluids toward the seafloor since it terminates upward in

214 chimney structures that are linked to surface gas seeps (Fig. 6).

215 Previous studies suggest that by comparing seismically derived chimney and fault probability cubes

216 it can be determined whether a fault or fracture is sealing or leaking (Ligtenberg, 2003; 2005). In this

217 study, we applied this method for fault seal analysis. High probability locations of chimneys (high

218 probability for fluid migration) are distributed along the NE-SW striking PR Fault zone, suggesting that

219 the PR Fault acts as a fluid pathway, whereas the NW-SE striking minor faults/fractures may not act as

220 good fluid conduits since they all show low probability for chimneys (Fig. 13). Ligtenberg (2005)

221 suggests that local dilatational zones are formed along the faults planes with orientations parallel/sub-

222 parallel to the main horizontal stress field (S_{Hmax}), while sealing faults orient normal to S_{Hmax}. These

223 observations may imply that the PR Fault is parallel/sub-parallel to the main horizontal stress field.

224 However, further evidence such as borehole data and geotechnical analysis is required on core samples

225 to test the hypothesis.

226

5.2 Pointer Ridge gas hydrate system

As a potential gas hydrate prospect, Pointer Ridge is characterized by active fluid flow, densely

distributed BSRs and incised channels that probably contain sandy turbidites. We propose a conceptual

model to illustrate the gas hydrate system (Fig. 14).

Several submarine channel systems exist on both sides of the PR Fault (Fig. 7). Since these channels

in the footwall of the PR Fault are caused by erosion in higher energy environments than the surrounding

contourites and levee deposits there is an increased probability that they contain more coarse-grained

sediments and would therefore make the best hydrate reservoirs in this geological setting (Figs. 7 and

14). Although there are high seismic amplitude anomalies indicating gas accumulation in the hanging

wall of the PR Fault, the potential turbidite sands cannot act as hydrate reservoirs but rather as potential

gas reservoirs as they are all situated deeper than the GHSZ (Figs. 7, 8 and 14).

The PR Fault and gas chimneys act as predominant conduits for fluids towards the GHSZ, with

some extending up to the seafloor. Due to the absence of large-scale fluid pathways, such as basement

faults, to transport fluids at depth toward the GHSZ, we suggest that shallow biogenic gas might be the

major source forming gas hydrates in the GHSZ, which is consistent with the geochemical (Chuang et

al., 2006; 2010) and geophysical (Sahoo et al., 2018) studies conducted in the SCS continental slope.

However, we cannot exclude the possibility of small amounts of thermogenic methane at this site.

Besides, strong gas accumulation in the hanging wall of the PR Fault (Figs. 6 and 14) suggests the fluid

migration along dipping sedimentary layers, which has been also investigated in Hikurangi margin

(Crutchley et al., 2018).

The near-vertical conduits for focused fluid flow in the subsurface, such as chimney or pipe

structures, are fractures created when the overpressure of fluids overcomes the tensile strength of the

surrounding rocks (Talukder et al., 2012). Studies conducted worldwide suggest that the development

of such fluid conduits can be greatly controlled by sedimentary and tectonic processes (Dugan and

Flemings, 2000; Tingay et al., 2007; Talukder et al., 2012). Erosion leads to the decrease of the

overburden stress and thus the strength of surrounding rocks, which requires lower overpressure to open

253 new fractures, while deposition increases the overburden stress, preventing fracture development. Our

254 results suggest that the fluid flow is more active in the footwall (erosional setting) than in the hanging

255 wall (depositional setting) of the PR Fault (Figs. 7; 8 and 12), which may indicate that erosional

256 processes triggered subsurface fluid flow and thus led to type I chimney development in the study area.

257

258 **6. Conclusions**

259   We have identified various features from seismic data that are related to specific interesting

260 geological processes in the Pointer Ridge area. Based on our observations, we propose a conceptual

261 model that illustrates the controlling mechanisms for the gas hydrate system in Pointer Ridge. As the

262 other ridges along the northern margin of the SCS slope have a similar geological setting it may be

263 expected that the findings for Pointer Ridge also apply there although deep-seated faults have not been

264 observed beneath the ridges further east. The results suggest that Pointer Ridge has all the elements

265 required as a potential gas hydrate prospect including a wide spread GHSZ, active fluid conduits that

266 penetrate the GHSZ and potential sandy reservoirs, but most of the promising targets currently lie below

267 the GHSZ. We summarize our results as follows:

268 1. Multi-attribute analysis can enhance subtle features, including paleo-channel deposits, chimneys and

269 faults, which would be missed in conventional seismic display. Results from neural network analysis

270 suggest that the NE-SW striking faults/fractures are active pathways for fluid migration, while those

271 aligned NW-SE are not.

272 2. Although the PR Fault is inactive at present, it is significant since clear variations of seafloor

273 topography, stratigraphy and fluid migration patterns are observed across it. Moreover, the PR Fault

274 acts as the primary fluid conduit that feeds gas-bearing fluids to the GHSZ, forming gas hydrates under

275 favorable conditions, in addition to the chimneys and dipping stratigraphic layers.

276 3. Results from seismic attribute analysis suggest that the paleo-channels are likely composed of sand-

277 rich turbidite deposits. We suggest that the paleo-channels located in the footwall of the PR Fault are

278 the best targets for future gas hydrate exploitation in the wider study area, while the paleo-channels

11

279 identified in the hanging wall of the PR Fault act as gas reservoirs instead of hydrate reservoirs, since

280 they are all deeper than the base of GHSZ.

281 4. Due to the reduced overburden, fluid flow is more active in the erosional environment than in the

282 depositional, indicating that the gas hydrate system can be greatly affected by varying sedimentary

283 processes in the study area.

284

285 **7. Acknowledgements**

294

8. References

295 **8.   References**

296 Aminzadeh, F., Connolly, D., Heggland, R., Meldahl, P., de Groot, P., 2002. Geohazard detection and

297   other applications of chimney cubes. The Leading Edge 21, 681–685.

298 Barnes, A., Cole, M., Michaels, T., Norlund, P., Sembroski, C., 2011. Making seismic data come alive.

299   First Break 29, 33–38.

300 Berndt, C., 2005. Focused fluid flow in passive continental margins. Philosophical Transactions of the

301   Royal Society of London A: Mathematical, Physical and Engineering Sciences 363, 2855–2871.

302 Berndt, C., Bünz, S., Mienert, J., 2003. Polygonal fault systems on the mid-Norwegian margin: a long-

303   term source for fluid flow. Geological Society, London, Special Publications 216, 283–290.

304 Berndt, C., Feseker, T., Treude, T., Krastel, S., Liebetrau, V., Niemann, H., Bertics, V.J., Dumke, I.,

305   Dünnbier, K., Ferré, B., 2014. Temporal constraints on hydrate-controlled methane seepage off

306   Svalbard. Science 1246298.

307 Boswell, R., Shipp, C., Reichel, T., Shelander, D., Saeki, T., Frye, M., Shedd, W., Collett, T.S.,

308   McConnell, D.R., 2016. Prospecting for marine gas hydrate resources. Interpretation 4, SA13–SA24.

309 Brouwer, F., Huck, A., 2011. An integrated workflow to optimize discontinuity attributes for the

310   imaging of faults, in: Attributes: New Views on Seismic Imaging—Their Use in Exploration and

311   Production. GCSSEPM, 31st Annual Conference Publication. p. 533.

312 Chen, L., Chi, W.-C., Liu, C.-S., Shyu, C.-T., Wang, Y., Lu, C.-Y., 2012. Deriving regional vertical

313   fluid migration rates offshore southwestern Taiwan using bottom-simulating reflectors. Marine

314   Geophysical Research 33, 379–388.

315 Chen, L., Chi, W.-C., Wu, S.-K., Liu, C.-S., Shyu, C.-T., Wang, Y., Lu, C.-Y., 2014. Two dimensional

316   fluid flow models at two gas hydrate sites offshore southwestern Taiwan. Journal of Asian Earth

317   Sciences 92, 245–253.

318 Chi, W., Reed, D.L., Tsai, C., 2006. Gas hydrate stability zone in offshore southern Taiwan. Terrestrial

319   Atmospheric and Oceanic Sciences 17, 829.

320   Chi, W.-C., Reed, D.L., Liu, C.-S., Lundberg, N., 1998. Distribution of the Bottom-Simulating

321   Reflector in the Offshore Taiwan Collision Zone. Terrestrial, Atmospheric and Oceanic Sciences 9,

322   779. https://doi.org/10.3319/TAO.1998.9.4.779(TAICRUST)

323   Chinwuko, A.I., Onwuemesi, A.G., Anakwuba, E.K., Onyekwelu, C.U., Okeke, H.C., Obiadi, I.I., 2015.

324   Coblending of seismic attributes for interpretation of channel geometries in Rence Field of Niger

325   Delta, Nigeria. Interpretation 3, T183–T195.

326   Chopra, S., Marfurt, K.J., 2011. Blended data renders visual value. AAPG Explorer/Geophysical Corner

327   3, 38–40.

328   Chopra, S., Marfurt, K.J., 2008. Emerging and future trends in seismic attributes. The Leading Edge 27,

329   298–318.

330   Chow, J., Lee, J.-S., Sun, R., Liu, C.S., Lundberg, N., 2000. Characteristics of the bottom simulating

331   reflectors near mud diapirs: offshore southwestern Taiwan. Geo-Marine Letters 20, 3–9.

332   Chuang, P.-C., Yang, T.F., Hong, W.-L., Lin, S., Sun, C.-H., Lin, A.-S., Chen, J.-C., Wang, Y., Chung,

333   S.-H., 2010. Estimation of methane flux offshore SW Taiwan and the influence of tectonics on gas

334   hydrate accumulation. Geofluids 10, 497–510.

335   Chuang, P.-C., Yang, T.-F., Lin, S., Lee, H.-F., Lan, T.F., Hong, W.-L., Liu, C.-S., Chen, J.-C., Wang,

336   Y.-S., 2006. Extremely high methane concentration in bottom water and cored sediments from

337   offshore southwestern Taiwan. Terrestrial.

338   Collett, T.S., 2012. Gas Hydrate Petroleum System Analysis, in: AGU Fall Meeting Abstracts.

339   Crutchley, G. J., Kroeger, K. F., Pecher, I. A., Gorman, A. R., 2018. How tectonic folding influences

340   gas hydrate formation: New Zealand's Hikurangi subduction margin. Geology, 47(1), 39-42.

341   Dalland, A., 1988. A lithostratigraphic scheme for the Mesozoic and Cenozoic succesion offshore

342   Norway north of 62° N. Norw. Petrol. Dir. Bull.

343   Dugan, B., Flemings, P.B., 2000. Overpressure and fluid flow in the New Jersey continental slope:

344   Implications for slope failure and cold seeps. Science 289, 288–291.

345   Feng, D., Chen, D., 2015. Authigenic carbonates from an active cold seep of the northern South China

346   Sea: new insights into fluid sources and past seepage activity. Deep sea research part II: topical

347   studies in oceanography 122, 74–83.

348   Ferguson, C.J., Avu, A., Paton, G.S., 2010. Seismic analysis workflow for reservoir characterization in

349   the vicinity of salt. first break 28.

350   Gay, A., Lopez, M., Cochonat, P., Séranne, M., Levaché, D., Sermondadaz, G., 2006. Isolated seafloor

351   pockmarks linked to BSRs, fluid chimneys, polygonal faults and stacked Oligocene–Miocene

352   turbiditic palaeochannels in the Lower Congo Basin. Marine Geology 226, 25–40.

353   Gay, A., Lopez, M., Cochonat, P., Sermondadez, G., 2004. Polygonal faults-furrows system related to

354   early stages of compaction-upper Miocene to recent sediments of the Lower Congo Basin. Basin

355   Research 16, 101–116.

356   Gay, A., Mourgues, R., Berndt, C., Bureau, D., Planke, S., Laurent, D., Gautier, S., Lauer, C., Loggia,

357   D., 2012. Anatomy of a fluid pipe in the Norway Basin: Initiation, propagation and 3D shape.

358   Marine Geology 332, 75–88.

359   Gong, C., Wang, Y., Peng, X., Li, W., Qiu, Y., Xu, S., 2012. Sediment waves on the South China Sea

360   Slope off southwestern Taiwan: implications for the intrusion of the Northern Pacific Deep Water

361   into the South China Sea. Marine and Petroleum Geology 32, 95–109.

362   Han, W.-C., 2017. Seismic Study on the Gas Hydrate Systems in the South China Sea Continental Slope

363   Offshore SW Taiwan. Doctoral Dissertation of Institute of Oceanography, National Taiwan

364   University, pp. 112 (in Chinese with English abstract).

365   Han, W.-C., Liu, C.-S., Chi, W.-C., Chen, L., Lin, C.-C., Chen, S.-C., 2017. Westward advance of the

366   deformation front and evolution of submarine canyons offshore of southwestern Taiwan. Journal of

367   Asian Earth Sciences 149, 6–19.

368   Hsu, H.-H., Liu, C.-S., Morita, S., Tu, S.-L., Lin, S., Machiyama, H., Azuma, W., Ku, C.-Y., Chen, S.-

369   C., 2017. Seismic imaging of the Formosa Ridge cold seep site offshore of southwestern Taiwan.

370   Marine Geophysical Research 1–13.

371 Huang, C.-Y., Wu, W.-Y., Chang, C.-P., Tsao, S., Yuan, P.B., Lin, C.-W., Xia, K.-Y., 1997. Tectonic

372   evolution of accretionary prism in the arc-continent collision terrane of Taiwan. Tectonophysics

373   281, 31–51.

374 Johnson, A.H., Max, M.D., 2006. The path to commercial hydrate gas production. The Leading Edge

375   25, 648–651.

376 Kvenvolden, K.A., 1998. A primer on the geological occurrence of gas hydrate. Geological Society,

377   London, Special Publications 137, 9–30.

378 Lester, R., Lavier, L.L., McIntosh, K., Van Avendonk, H.J., Wu, F., 2012. Active extension in Taiwan's

379   precollision zone: A new model of plate bending in continental crust. Geology 40, 831–834.

380 Li, C.-F., Zhou, Z., Li, J., Hao, H., Geng, J., 2007. Structures of the northeasternmost South China Sea

381   continental margin and ocean basin: geophysical constraints and tectonic implications. Marine

382   Geophysical Researches 28, 59–79.

383 Li, L., Lei, X., Zhang, X., Sha, Z., 2013. Gas hydrate and associated free gas in the Dongsha Area of

384   northern South China Sea. Marine and Petroleum Geology 39, 92–101.

385 Liao, W.-Z., Lin, A.T., Liu, C.-S., Oung, J.-N., Wang, Y., 2016. A study on tectonic and sedimentary

386   development in the rifted northern continental margin of the South China Sea near Taiwan.

387   Interpretation 4, SP47–SP65.

388 Liao, W.-Z., Lin, A.T., Liu, C.-S., Oung, J.-N., Wang, Y., 2014. Heat flow in the rifted continental

389   margin of the South China Sea near Taiwan and its tectonic implications. Journal of Asian Earth

390   Sciences 92, 233–244.

391 Ligtenberg, J.H., 2005. Detection of fluid migration pathways in seismic data: implications for fault

392   seal analysis. Basin Research 17, 141–153. https://doi.org/10.1111/j.1365-2117.2005.00258.x

393 Ligtenberg, J.H., 2003. Unravelling the petroleum system by enhancing fluid migration paths in seismic

394   data using a neural network based pattern recognition technique. Geofluids 3, 255–261.

395 Lin, A.T., Watts, A., Hesselbo, S.P., 2003. Cenozoic stratigraphy and subsidence history of the South

396   China Seamargin in the Taiwan region. Basin Research 15, 453–478.

397   Lin, C.-C., Lin, A.T.-S., Liu, C.-S., Chen, G.-Y., Liao, W.-Z., Schnurle, P., 2009. Geological controls

398   on BSR occurrences in the incipient arc-continent collision zone off southwest Taiwan. Marine and

399   Petroleum Geology 26, 1118–1131.

400   Lin, C.-C., Lin, A.T.-S., Liu, C.-S., Horng, C.-S., Chen, G.-Y., Wang, Y., 2014. Canyon-infilling and

401   gas hydrate occurrences in the frontal fold of the offshore accretionary wedge off southern Taiwan.

402   Marine Geophysical Research 35, 21–35.

403   Lin, L.H., Chiu, J.H., Wu, S.H., 1993. The hydrocarbon generation and migration study in the Central

404   Uplifted Zone, Tainan Basin. Bull. Explor. Prod. Res. CPC Corp 16, 349–369.

405   Liu, C.-S., Huang, I.L., Teng, L.S., 1997. Structural features off southwestern Taiwan. Marine Geology

406   137, 305–319.

407   Liu, C.-S., Liu, S.-Y., Lallemand, S.E., Lundberg, N., Reed, D.L., 1998. Digital elevation model

408   offshore Taiwan and its tectonic implications. Terrestrial, Atmospheric and Oceanic Sciences 9,

409   705–738.

410   Liu, C.-S., Wang, Y.-S., Chung, S.-H., Chen, S.-C., Hsiuan, T.-H., 2006. Distribution and characters of

411   gas hydrate offshore of southwestern Taiwan. Terrestrial.

412   Lundberg, N., Reed, D.L., Liu, C.-S., Jr Lieske, L., 1992. Structural Controls on Orogenic

413   Sedimentation Submarine Taiwan Collision. Acta Gelological Taiwanica 131–140.

414   Max, M.D., Johnson, A.H., 2014. Hydrate petroleum system approach to natural gas hydrate exploration.

415   Petroleum Geoscience 2012–049.

416   McDonnell, S.L., Max, M.D., Cherkis, N. e a1, Czarnecki, M.F., 2000. Tectono-sedimentary controls

417   on the likelihood of gas hydrate occurrence near Taiwan. Marine and Petroleum Geology 17, 929–

418   936.

419   Meldahl, P., Heggland, R., Bril, B., de Groot, P., 2001. Identifying faults and gas chimneys using

420   multiattributes and neural networks. The Leading Edge 20, 474–482.

421   Nixon, M.F., Grozic, J.L., 2007. Submarine slope failure due to gas hydrate dissociation: a preliminary

422   quantification. Canadian Geotechnical Journal 44, 314–325.

423   Qayyum, F., de Groot, P., 2012. Seismic dips help unlock reservoirs. American Oil & Gas Reporter 60,

424   75–79.

425   Reed, D.L., Lundberg, N., Liu, C.-S., Kuo, B.-Y., 1992. Structural Relations along the Margins of the

426   Offshore Taiwan Accrentionary Wedge: Implications for Accretion and Crustal Kinematics. Acta

427   Gelological Taiwanica 105–122.

428   Ru, K., Pigott, J.D., 1986. Episodic rifting and subsidence in the South China Sea. AAPG Bulletin 70,

429   1136–1155.

430   Ruppel, C.D., 2011. Methane hydrates and contemporary climate change. Nature Education Knowledge

431   3.

432   Sahoo, S.K., Chi, W.-C., Han, W.-C., Chen, L., Liu, C.-S., Wang, Y., 2018. Estimating the composition

433   of gas hydrate using 3D seismic data from Penghu Canyon, offshore Taiwan. Terrestrial,

434   Atmospheric and Oceanic Sciences 29, 105–115.

435   Schnürle, P., Hsiuan, T.H., Liu, C.-S., 1999. Constrains on free gas and gas hydrate bearing sediments

436   from multi-channel seismic data, offshore southwestern Taiwan. Petrol. Geol. Taiwan 33, 21–42.

437   Shyu, C.-T., Hsu, S.-K., Liu, C.-S., 1998. Heat Flows off Southwest Taiwan: Measurements over Mud

438   Diapirs and Estimated from Bottom Simulating Reflectors. TAO 9, 795–812.

439   Sloan, E.D.J., 1998. Physical/chemical properties of gas hydrates and application to world margin

440   stability and climatic change. Geological society, London, special publications 137, 31–50.

441   Sun, Q., Wu, S., Cartwright, J., Dong, D., 2012. Shallow gas and focused fluid flow systems in the Pearl

442   River Mouth Basin, northern South China Sea. Marine Geology 315, 1–14.

443   Talukder, A.R., 2012. Review of submarine cold seep plumbing systems: leakage to seepage and

444   venting. Terra Nova 24, 255–272.

445   Taner, M.T., 2001. Seismic attributes. CSEG recorder 26, 49–56.

446   Tingay, M.R., Hillis, R.R., Swarbrick, R.E., Morley, C.K., Damit, A.R., 2007. 'Vertically

447   transferred' overpressures in Brunei: Evidence for a new mechanism for the formation of high-

448   magnitude overpressure. Geology 35, 1023–1026.

449   Tingdahl, K.M., De Rooij, M., 2005. Semi-automatic detection of faults in 3D seismic data.

450   Geophysical prospecting 53, 533–542.

451   Yan, P., Deng, H., Liu, H., 2006. The geological structure and prospect of gas hydrate over the Dongsha

452   Slope, South China Sea. Terrestrial Atmospheric and Oceanic Sciences 17, 645.

453   Yang, K.M., Ting, H.H., Yuan, J., 1991. Structural styles and tectonic modes of Neogene extensional

454   tectonics in southwestern Taiwan: Implications for hydrocarbon exploration. Petroleum Geology of

455   Taiwan 26, 1–31.

456   Yeh, Y.-C., Hsu, S.-K., Doo, W.-B., Sibuet, J.-C., Liu, C.-S., Lee, C.-S., 2012. Crustal features of the

457   northeastern South China Sea: insights from seismic and magnetic interpretations. Marine

458   Geophysical Research 33, 307–326.

459   Yu, H.-S., 2004. Nature and distribution of the deformation front in the Luzon Arc-Chinese continental

460   margin collision zone at Taiwan. Marine Geophysical Researches 25, 109–122.

461   Yu, X., Liang, J., Fang, J., Cong, X., Jiang, L., Wang, J., 2012. Tectonic subsidence characteristics and

462   its relationship to BSR distribution in deep water area of Pearl River Mouth Basin since the Late

463   Miocene. Journal of Palaeogeography 14, 787–800.

464   Zhang, G., Liang, J., Lu, J., Yang, S., Zhang, M., Holland, M., Schultheiss, P., Su, X., Sha, Z., Xu, H.,

465   2015. Geological features, controlling factors and potential prospects of the gas hydrate occurrence

466   in the east part of the Pearl River Mouth Basin, South China Sea. Marine and Petroleum Geology

467   67, 356–367.

468   Zhang, G.X., Yang, S.X., Zhang, M., Liang, J.Q., Lu, J., Holland, M., 2014. GMGS2 expedition

469   investigates rich and complex gas hydrate environment in the South China Sea. Center for Natural

470   Gas and Oil 412, 386–7614.

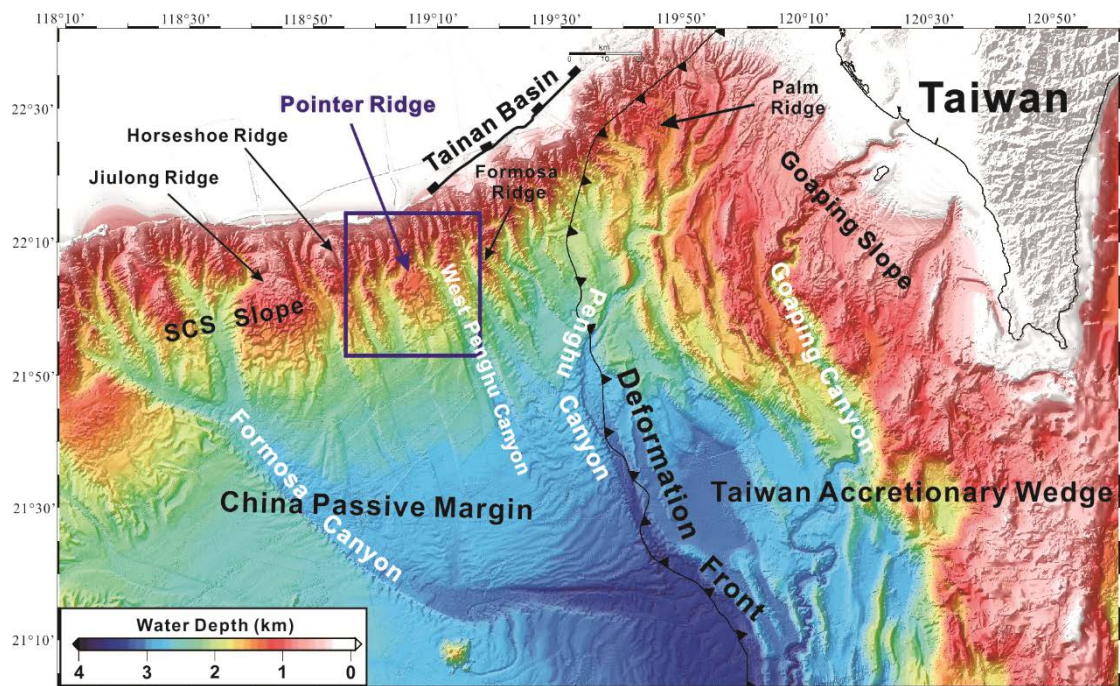471

Figures and figure captions

474   Fig. 1. Bathymetric map showing major tectonic structures and submarine canyons offshore SW Taiwan.

475   The black box indicates the study area. The black line with teeth show the location of deformation front
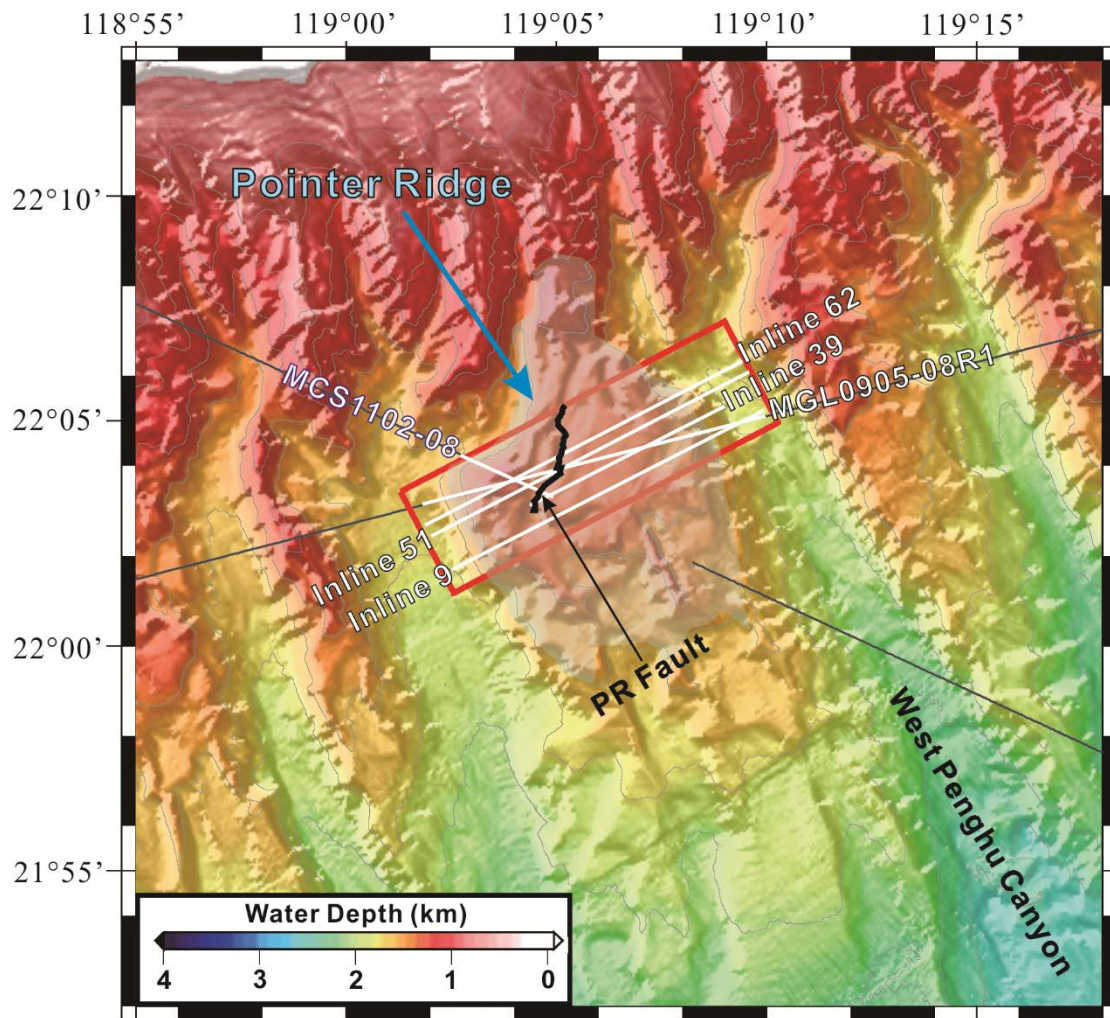
476   (Han et al., 2017).

Fig. 2. Bathymetric map showing distributions of the seismic data, PR fault, chimneys and gas plume sites in the study area. The red box indicates the 3D seismic survey area; the black lines show the location of available 2D seismic data; the white lines are seismic sections shown in this study.

481
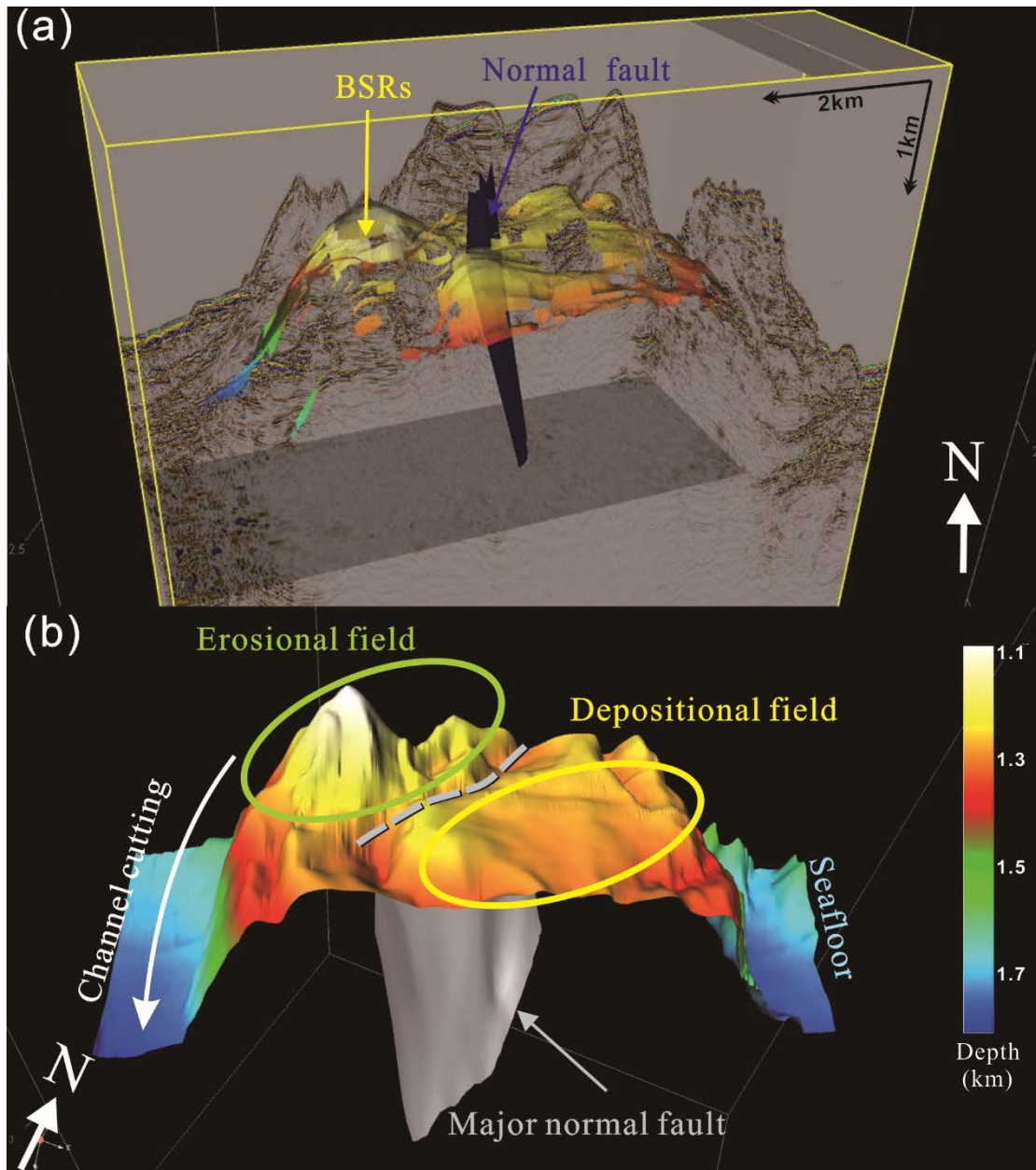
Fig. 3. (a) 3D Seismic volume and 3D geometries of the BSRs and the PR Fault in the 3D cube; (b) 3D

bathymetry display which shows different sedimentary settings across the PR Fault.

484
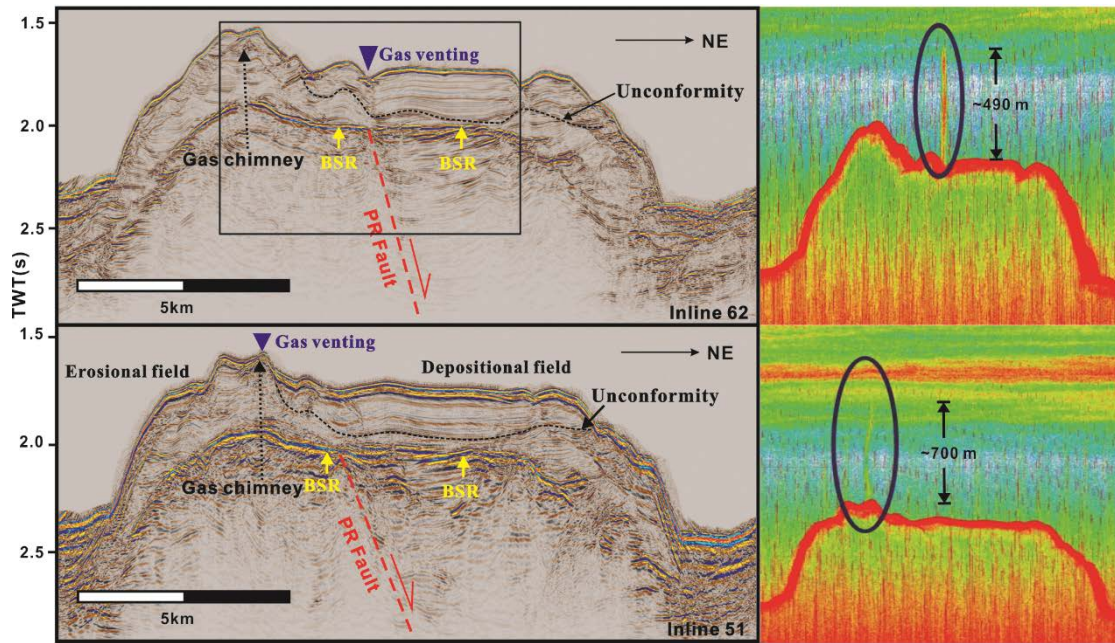
Fig. 4. Interpreted seismic inline profiles 62 and 51 and their corresponding water column images showing correlation of gas venting sites and subsurface fluid conduits. The black box indicates the location of Fig. 6.

488
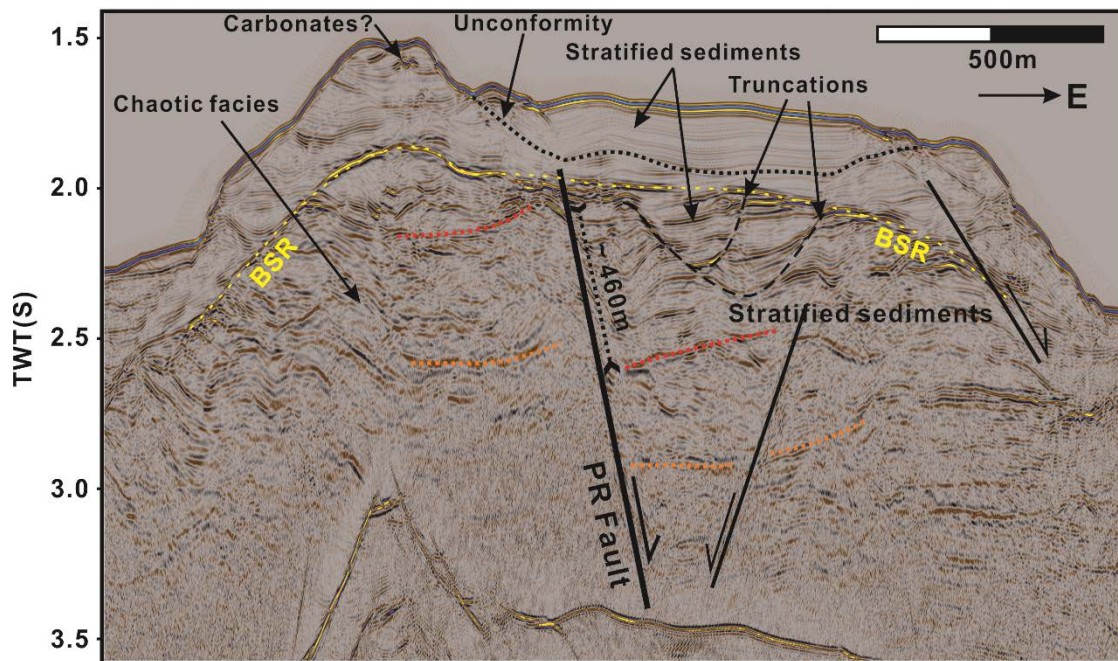
Fig. 5. Interpreted seismic profile MGL0905-08R1 showing the structural and sedimentary features in the Pointer Ridge. An offset around 460 m across the PR Fault is revealed by strata marked by the red and the orange lines.

492
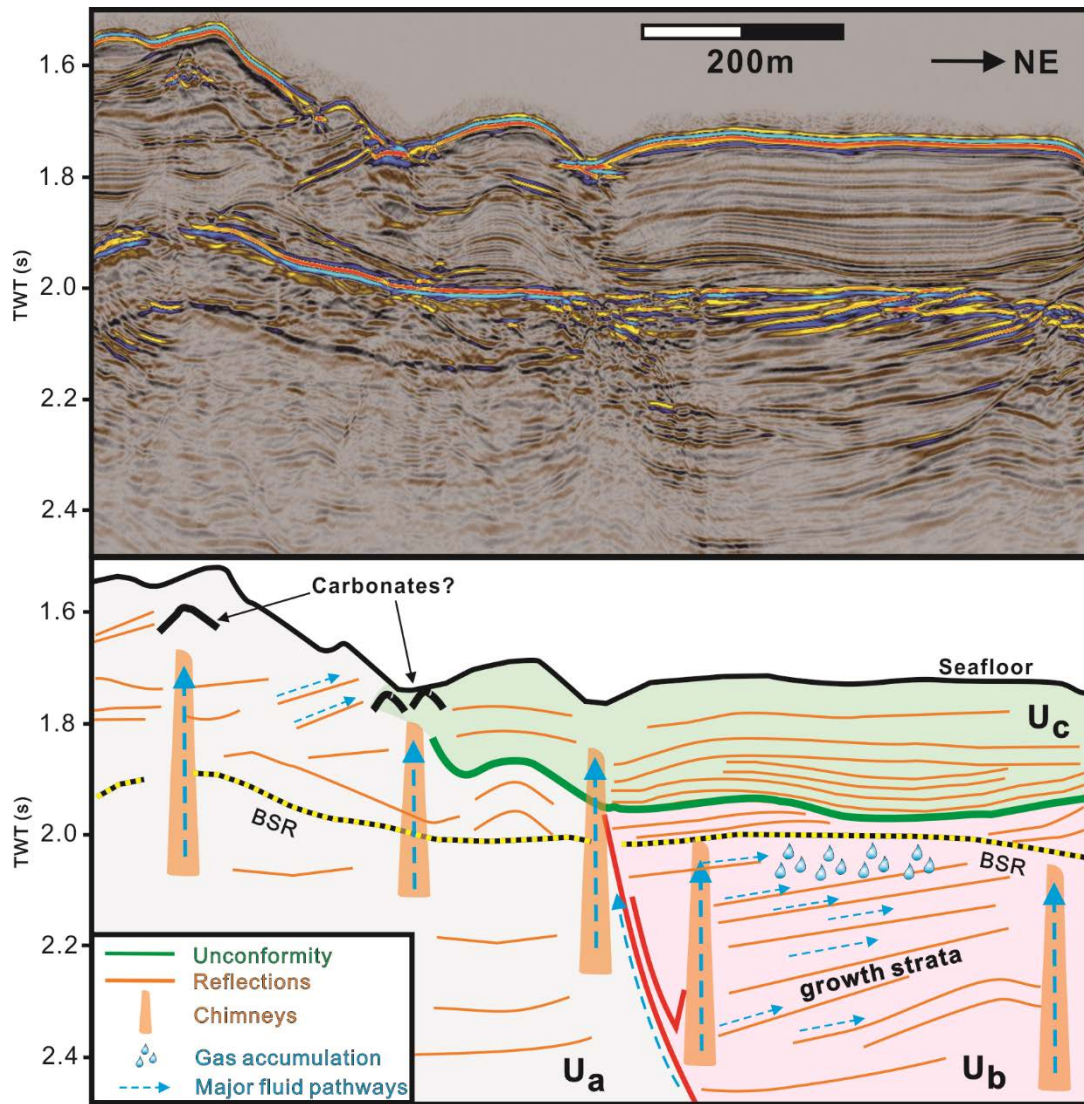
493   Fig.6. Interpretation of seismic inline profile 62. Three seismic units Ua (grey), Ub (pink), and Uc

494   (green) are interpreted as pre-faulting, syn-faulting and post-faulting deposits, respectively.

495
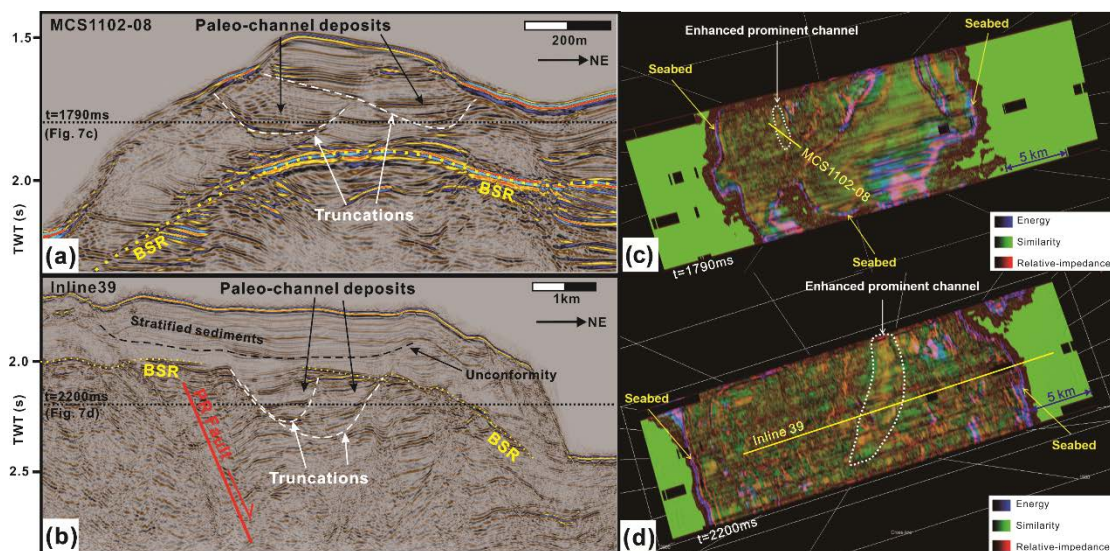
496   Fig. 7. Examples showing turbidite channel sands identified from seismic sections (a and b) and co-

497   blending of seismic attributes (c and d).
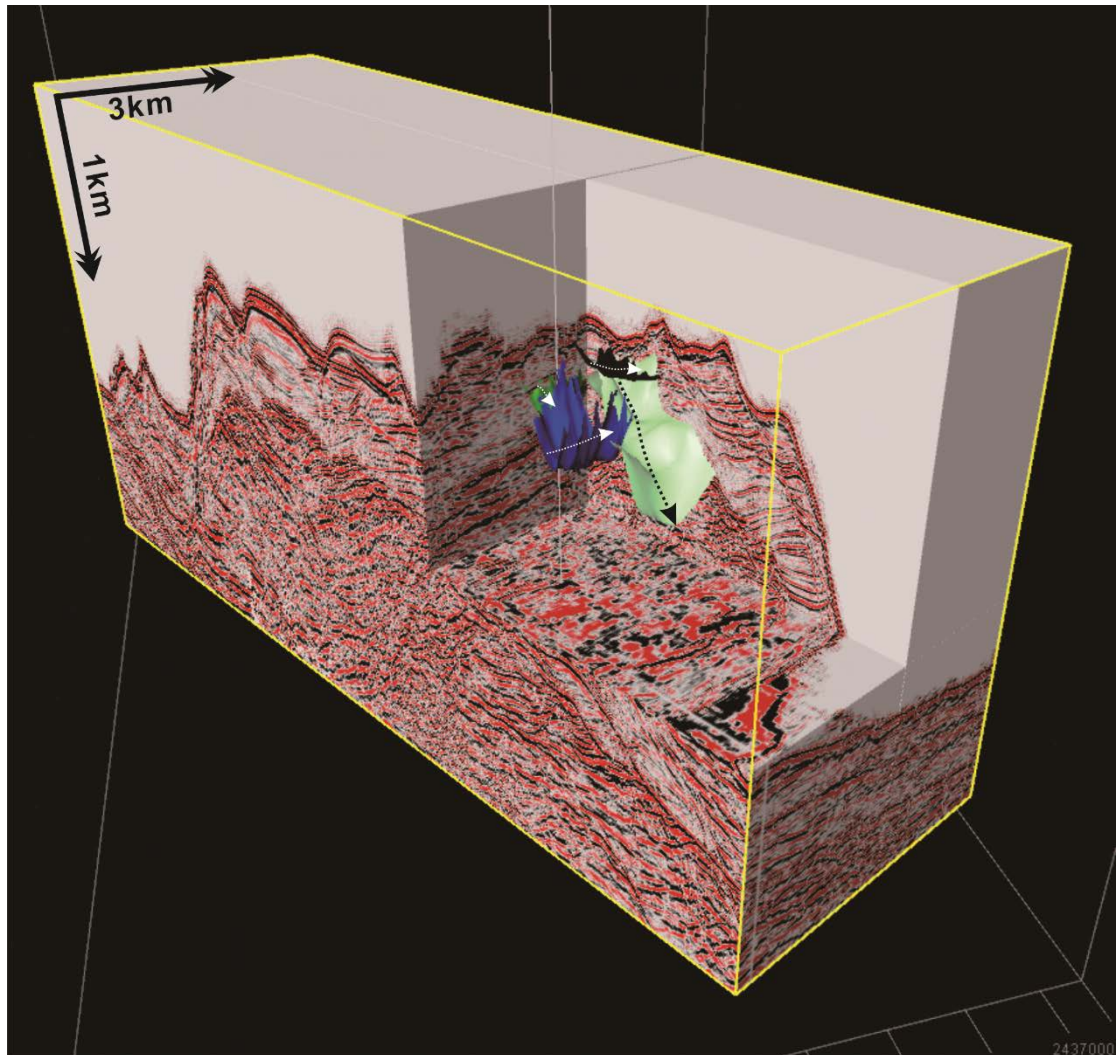
498

499   Fig. 8. Perspective view of the 3D seismic cube showing the distribution of buried canyons located in

500   the GHSZ that are potential sandy gas hydrate reservoirs. Arrows indicate the thalweg of the buried

501   canyons.

502
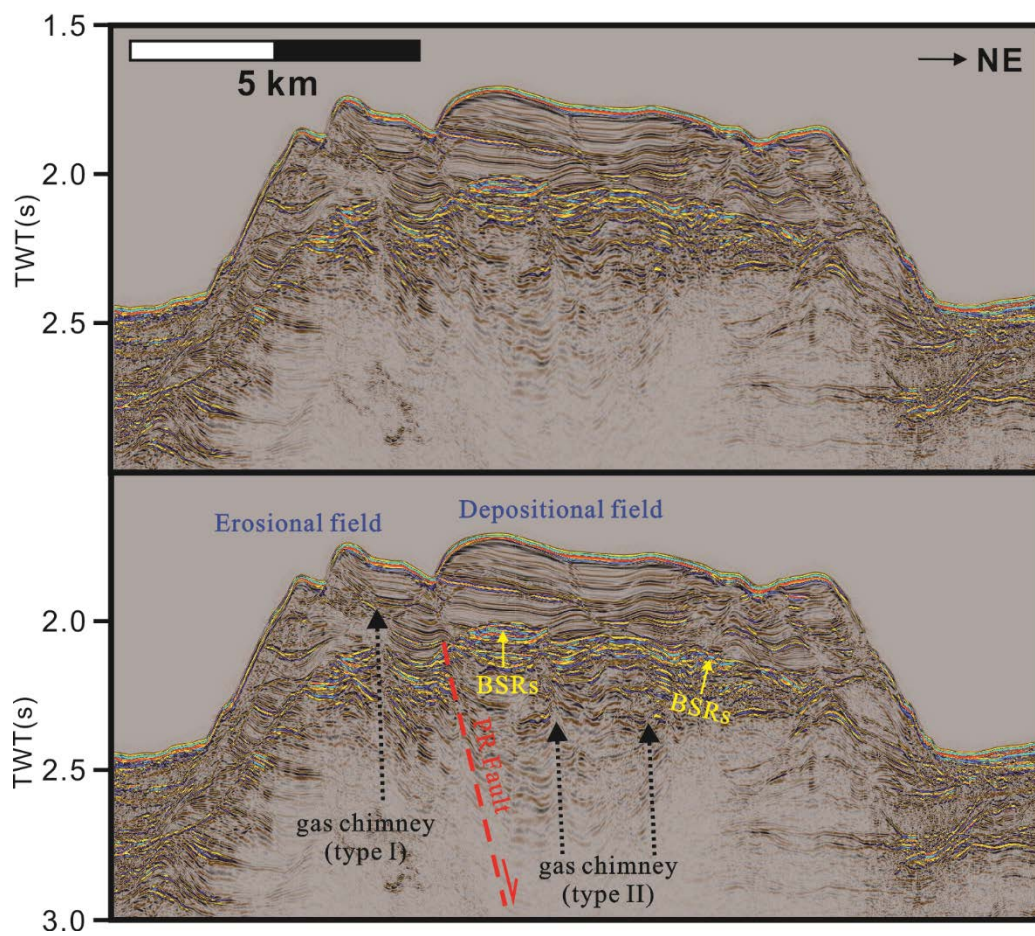
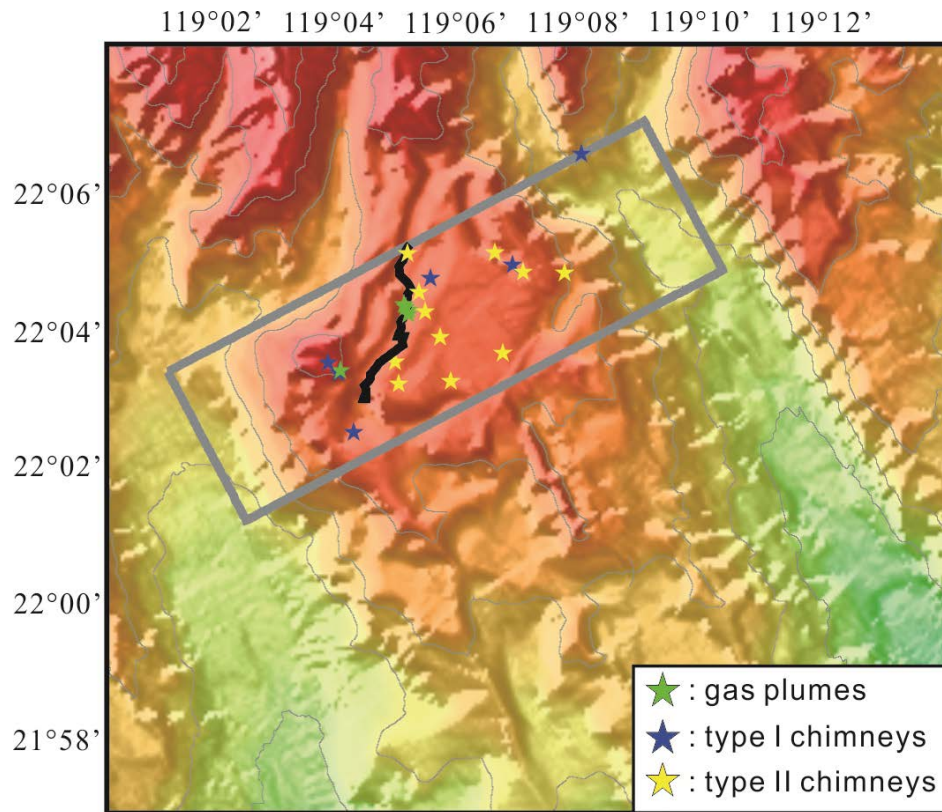Fig. 9. Interpreted seismic inline profile 9 presenting different chimney types across the PR Fault.

Fig. 10. Seepage related feature distribution at Pointer Ridge. The grey box indicates the 3D seismic survey area; the black line shows the location of the PR Fault; the green stars are location of gas venting sites imaged from water column data; the blue and yellow stars indicate the type I and type II chimneys respectively. For bathymetry legend please refer to Fig. 1.
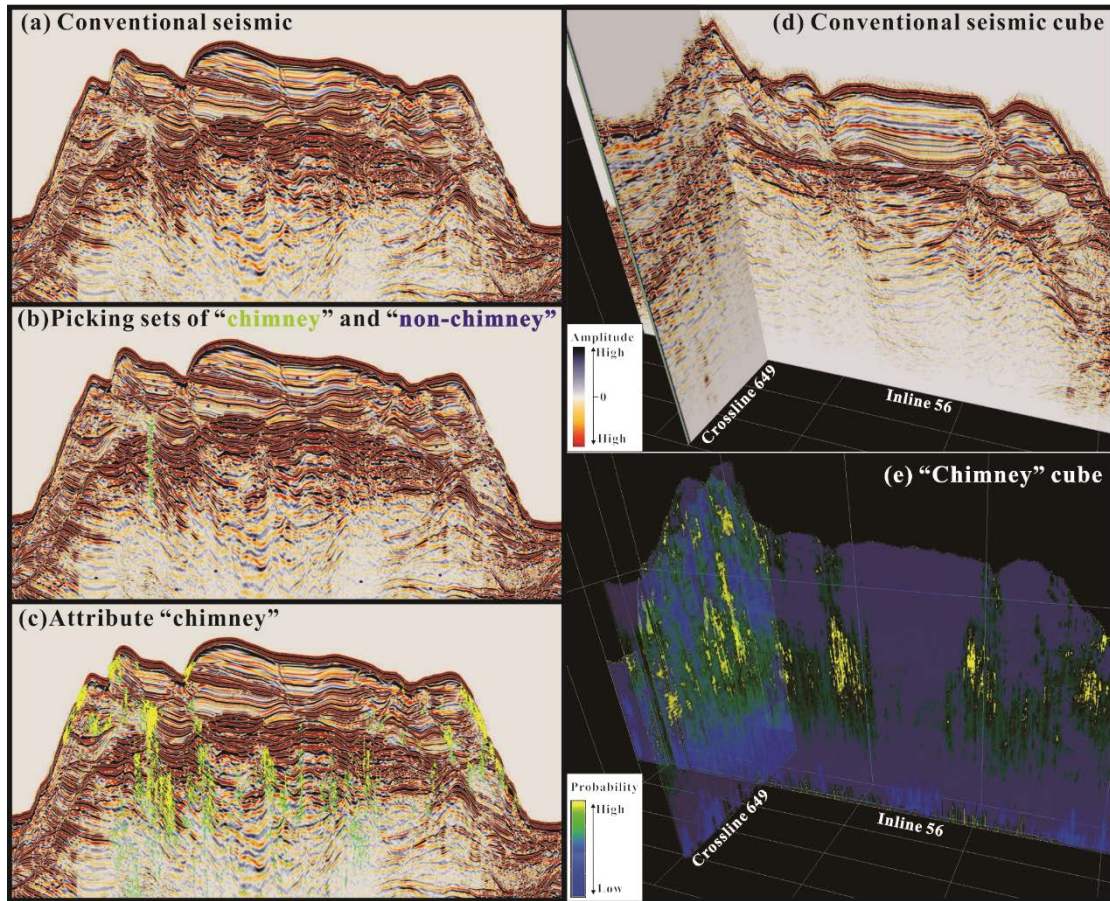
509

Fig. 11. Inline 9 seismic profile (left) and 3D perspective display of inline 56 and crossline 649 in 3D

(right) showing (a) conventional seismic image; (b) input picking sets for neural networks; (c) attribute

"chimney"; (d) conventional seismic; and (e) attribute "chimney". Green and violet points in (b)

indicate the "chimney" and "non-chimney" locations, respectively. Green and yellow areas in (c) and

(e) indicate the high probability "chimney" locations. See Fig. 2 for location of inline 9.
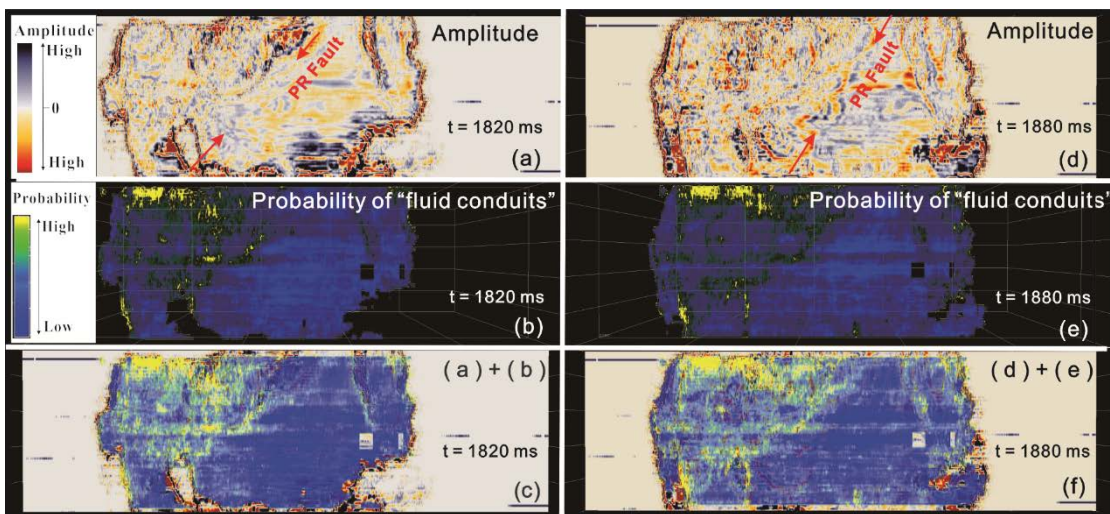

515

Fig. 12. Time slices extracted from 3D conventional seismic and chimney cubes showing the fluid migration patterns across the PR Fault. (a) time slice (1820 ms, TWT) of the conventional seismic cube showing the location of PR Fault; (b) time slice (1820 ms, TWT) of the chimney cube; (c) co-blending of time slices (1820 ms, TWT) of the conventional seismic cube and the chimney cube; (d) time slice (1880 ms, TWT) of the conventional seismic cube showing the location of PR Fault; (e) time slice (1880 ms, TWT) of the chimney cube; (f) co-blending of time slices (1880 ms, TWT) of the conventional seismic cube and the chimney cube. Please note that overall the signal of fluid migration in the footwall (upper left) of the PR Fault is stronger than that in its footwall (lower right).
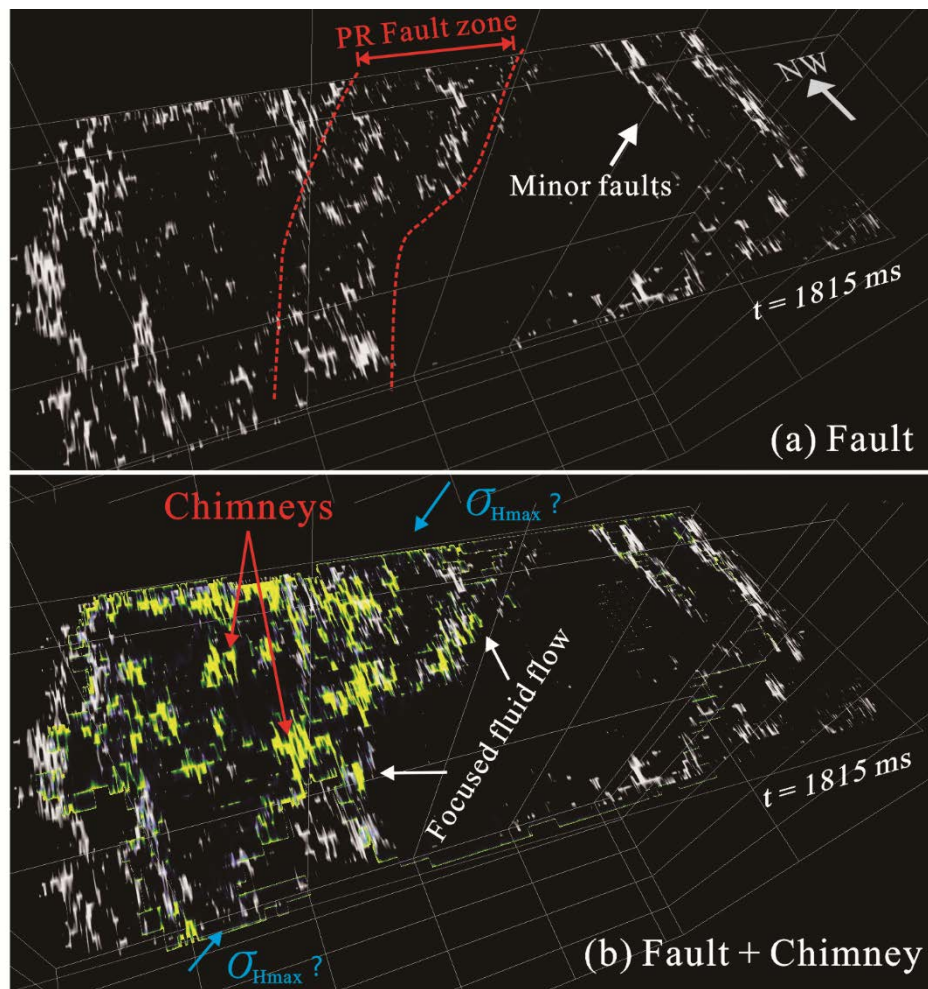

Fig. 13 (a) Time slice of the fault cube showing high probability fault/fracture locations (white); (b) co-blending of time slices of the fault cube and the chimney cube. High probability chimney locations (shown in yellow) mainly distribute along the PR Fault zone and its footwall (NW).
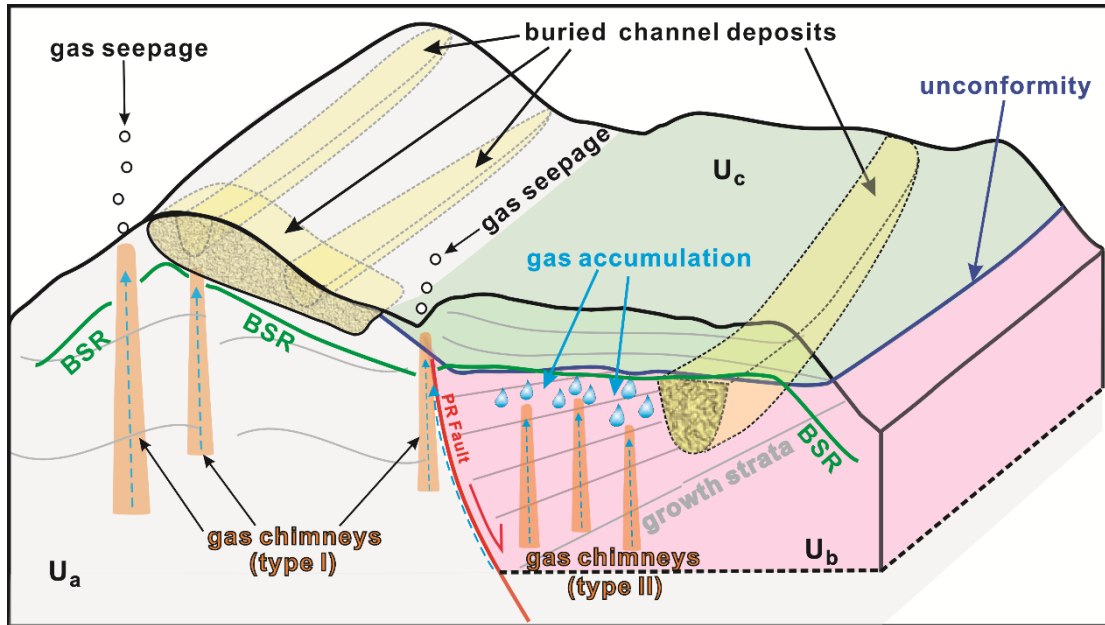
528

529   Fig. 14. Conceptual model illustrating the gas hydrate system of the Pointer Ridge. Stratigraphic settings,

530   fluid migration patterns and hydrate reservoir characteristics of Pointer Ridge are illustrated.

531

532   Table 1. Acquisition parameters of the seismic survey systems used in this study.

Cruise	MCS1083	MCS1089	MCS1102	MGL0905
Source	2 air guns	2 air guns	3 air guns	large (40guns) air gun array
Source volume	450 in.^{3}	450 in.^{3}	775 in.^{3}	6000 in.^{3}
No. channels	108	108	108	468
Channel interval	12.5	12.5	12.5	12.5
Acquisition vessel	R/V OR1	R/V OR1	R/V OR1	R/V Marcus G. Langseth

533

534   Table 2. Geometry parameter of the 3D seismic cube used in this study.

Parameters	Inline No.	Inline spacing	Xline No.	Xline spacing
	95	50m	2400	6.25m

535